

Modeling and Analysis of Ultrasound Backscattering by Spherical Aggregates and Rouleaux of Red Blood Cells

Beng-Ghee Teh and Guy Cloutier, *Member, IEEE*

Abstract—The present study concerns the modeling and analysis of ultrasound backscattering by red blood cell (RBC) aggregates, which under pathological conditions play a significant role in the rheology of blood within human vessels. A theoretical model based on the convolution between a tissue matrix and a point spread function, representing, respectively, the RBC aggregates and the characteristics of the ultrasound system, was used to examine the influence of the scatterer shape and size on the backscattered power. Both scatterers in the form of clumps of RBC aggregates and rouleaux were modeled. For all simulations, the hematocrit was kept constant at 10%, the ultrasound frequency was 10 MHz, the insonification angle was varied from 0 to 90°, and the scatterer size (diameter for clumps and length for rouleaux) ranged from 4 μm to 120 μm . Under Rayleigh scattering by assuming a Poisson distributed scatterers in space, the ultrasound backscattered power increased linearly with the particle volume. For non-Rayleigh scatterers, the intensity of the echoes diminished as the scatterer volume increased, with the exception of rouleaux at an angle of 90°. As expected, the backscattered power was angular dependent for anisotropic particles (rouleaux). The ultrasound backscattered power may not always increase with the size of the aggregates, especially when they are no longer Rayleigh scatterers. In the case of rouleaux, the anisotropy of the backscattered power is emphasized in the non-Rayleigh region.

I. INTRODUCTION

UNDER normal physiological conditions, the red blood cells (RBCs) may aggregate into stacks called rouleaux, which is a result of the interaction between plasma proteins and the RBC membrane. The rouleaux may further interact with other rouleaux to form rouleau networks, depending on the flow conditions, cellular factors, and the blood plasma protein content. Clumps of RBCs can be found under human pathological conditions. Aggregates formed in stationary flow or low flow conditions disaggregate at higher flow rates due to the increase in shear forces. Because RBC aggregation is a reversible process, reducing the shear forces results in the reaggregation of RBCs. Under pathological conditions in which

RBC aggregability is elevated, the rate of aggregate formation and the adhesive strength between RBCs are increased. Pathological levels of RBC aggregation play a role in microcirculatory flow disorders and vascular thrombosis [1], [2].

Several research groups have shown that ultrasound backscattering is sensitive to the presence of RBC aggregation [3]. The ultrasonic backscatter from flowing whole blood was found to be different from that of RBC saline suspensions (no aggregation) in that the former is shear rate dependent [4]. These last experiments were conducted with animal blood from different species, and the results pointed to a species-dependent backscatter that could be explained based on the degree of aggregation of the species' blood sample. The same group also showed that ultrasonic backscatter from flowing whole blood was dependent on the concentration of fibrinogen (a plasma protein that strongly promotes RBC aggregation) [5]. Kim *et al.* [6] demonstrated that the ultrasonic backscattered intensity increased after the human blood sample in an oscillatory flow was abruptly stopped. They also observed a rapid decrease in echo intensity when the flow was resumed. Boynard and Lelièvre [7] used ultrasound to measure the backscattering intensity of a RBC dextran suspension. They made an attempt to relate the mean size of RBC aggregates to the backscattered intensity.

Ultrasonic backscattered power from asymmetric scatterers with size in the range of the wavelength has been shown to be angular dependent, in which the angle is between the ultrasonic beam and the longitudinal axis of the scatterers. Some examples of such observation can be found in experiments conducted with myocardial tissue [8], bovine liver [9], human Achilles tendon [10], and renal parenchyma [11]. All of the results showed a maximum ultrasonic backscatter when the direction of the ultrasonic beam was perpendicular to the longitudinal axis of the scatterers, and a minimum when the beam direction was parallel to their long axis. Such anisotropic behavior also was observed in flow experiments conducted with porcine whole blood, as well as with carbon fibers suspended in a saline-glycerol solution [12]. Each carbon fiber was approximately 7 μm in diameter and 250 μm in length, mimicking a long rouleau of RBCs. In this last study, the anisotropy was not observed for porcine RBCs suspended in a saline solution, in which scatterers existed in the form of individual RBCs not forming aggregates, and for conditions in which clumps were expected.

Manuscript received June 4, 1999; accepted February 21, 2000. This work was supported by a research scholarship from the Fonds de la Recherche en Santé du Québec (to G.C.), and by grants from the Medical Research Council of Canada (#MT-12491 and #MOP-36467) and the Heart and Stroke Foundation of Quebec.

B. G. Teh is with Cypress Semiconductor, San José, CA.

G. Cloutier is with the Laboratory of Biomedical Engineering, Institut de recherches cliniques de Montréal, Montreal, P.Q., H2W 1R7, Canada (e-mail: cloutig@ircm.qc.ca).

In summary, a correlation exists between the size and orientation of RBC aggregates, and the ultrasonic backscattered power. When the blood sample is in motion, the shearing effects of the flow cause the RBC aggregates to break apart, leading to smaller aggregates and weaker backscattered power. Conversely, when the flow is ceased or reduced, the shearing effects decay accordingly, consequently, the RBCs reaggregate, which is reflected by a stronger backscattered power and possible anisotropy. Blood samples with little or no aggregates, such as bovine whole blood or RBCs suspended in a saline solution, are independent of the shearing effects of the flow under laminar flow, and the backscattered power is not influenced by the angle.

According to the Rayleigh scattering theory [13], the power backscattered by one particle (backscattering cross section) depends on the square of the particle volume. However, at a constant hematocrit, the ultrasound backscattered power is expected to be proportional to the mean aggregate's volume [14]. This situation should exist if scatterers are small enough to satisfy the Rayleigh scattering condition, and if their spatial arrangement (packing factor) is unchanged when the volume of the aggregates is increased. From this discussion, it is clear that the ultrasound backscattered power can be used as a signature to study RBC aggregation. However, although it is known from the literature that RBC aggregation increases ultrasound backscattering, the exact mechanism by which the power is increased is unknown. The volume of the aggregates certainly has an effect, but other factors—such as the hematocrit, the manner in which RBCs are packed, the shape of the aggregates, their variance in size, and the fluctuation of all these parameters in time and space—may all contribute. In the present study, the influence of the volume and shape of the aggregates was specifically addressed with a theoretical simulation at various insonification angles.

II. METHOD

A. The Model

A linear model was developed to study ultrasound backscattering by spherical aggregates and rouleaux of RBCs. A similar model recently was used to simulate the ultrasonic signal backscattered by nonaggregating RBCs [14]. A strength of the model is the possibility to consider the effect of acoustic interference on the backscattered power. The model takes into account interference between echoes from all point sources sampled within each scatterer. This allows modeling of both Rayleigh and non-Rayleigh scattering conditions. The model uses the Born approximation, which implies that the scattered echoes are weak compared to the incident signal. The backscattered radio-frequency (RF) signal from a volume of interest

(VOI), $RF_{3D}(x, y, z)$, can be expressed as:

$$RF_{3D}(x, y, z) = \frac{\partial^2}{\partial y^2} T_{3D}(x, y, z) \otimes Z_{3D}(x, y, z), \quad (1)$$

where $T_{3D}(x, y, z)$ is the three-dimensional (3-D) point spread function (PSF) of the ultrasound system, \otimes denotes the convolution operation, and $Z_{3D}(x, y, z)$ is the acoustic impedance function that considers the scatterer's shape, size, and spatial arrangement. The variable y refers to the direction of propagation of the pressure waves, and x and z are along the lateral and elevation directions, respectively. The second order derivative with respect to y considers the fluctuations in acoustic impedance of the medium (fluctuations in density and compressibility).

For the ease of computation, we consider a single slice of the 3-D RF signal (obtained from all scatterers in the VOI), $RF_{2D}(x, y) = RF_{3D}(x, y, 0)$. If $T_{3D}(x, y, z)$ is separable, that is, $T_{3D}(x, y, z) = T(x, y)T_z(z)$, (1) simplifies to a 2-D convolution:

$$RF_{2D}(x, y) = \frac{\partial^2}{\partial y^2} T(x, y) \otimes Z(x, y), \quad (2)$$

$$\text{where } Z(x, y) = \int_z T_z(-z)Z_{3D}(x, y, z) dz. \quad (3)$$

In (3), $Z(x, y)$ is the projection of the 3-D impedance function weighted by $T_z(-z)$.

Because the region of interest is composed of a collection of scatterers, the tissue impedance, $Z_{3D}(x, y, z)$, can be assumed to be an ensemble of small scatterer inhomogeneities:

$$Z_{3D}(x, y, z) = \int_n Z_n(x, y, z), \quad (4)$$

where n indicates the n^{th} scatterer in the VOI. If scatterers all have the same size and shape, then only a universal scatterer prototype is required to generate $Z(x, y)$. In that case, a scatterer prototype function can be defined and repeated at each scatterer position, i.e.:

$$Z_n(x, y, z) = a_n C_{3D}(x - x_n, y - y_n, z - z_n), \quad (5)$$

where a_n represents the echogenicity of the n^{th} scatterer, and $C_{3D}(\cdot)$ is the scatterer prototype function. Substituting (5) into (4) and then into (3) gives:

$$Z(x, y) = \int_z \sum_n a_n T_z(-z) C_{3D}(x - x_n, y - y_n, z - z_n) dz. \quad (6)$$

When the scatterer size is small compared to the thickness of the beam in the z direction, the value of $T_z(-z)$ remains constant within each scatterer volume. With respect to each scatterer, this implies that $T_z(-z)$ varies

only from scatterer to scatterer and not in the z direction within any particular scatterer location. Therefore, $T_z(-z)$ can be taken out of the integral, which results in:

$$\begin{aligned} Z(x, y) &= \sum_n a_n T_z(-z_n) \int_z C_{3D} \\ &\quad (x - x_n, y - y_n, z - z_n) dz \\ &= \sum_n a_n T_z(-z_n) C(x - x_n, y - y_n), \end{aligned} \quad (7)$$

$$\text{where } C(x, y) = \int_z C_{3D}(x, y, z) dz. \quad (8)$$

This means that the 2-D tissue impedance function $Z(x, y)$ can be generated by projecting the scatterer prototype function along the z -axis, then weighting the result with $T_z(-z_n)$ at each scatterer location. $Z(x, y)$ also can be expressed as the 2-D convolution between $C(x, y)$ and a position matrix $N(x, y)$:

$$Z(x, y) = C(x, y) \otimes N(x, y), \quad (9)$$

$$\text{where } N(x, y) = \sum_n a_n T_z(-z_n) \delta(x - x_n, y - y_n). \quad (10)$$

$N(x, y)$ is essentially a matrix with randomly positioned Dirac delta functions weighted by $T_z(-z_n)$ and a_n , that describes the spatial arrangement of scatterers. With the model of (1), the scattering arrangement in space is determined by the statistical model used to describe $N(x, y, z)$. Based on (9) one will get an "ideal" tissue matrix, in which all scatterers simulated have the same size, shape, and orientation. Having obtained $Z(x, y)$, the 2-D RF image, $RF_{2D}(x, y)$, can be computed according to (2).

B. Main Assumptions of the Model

The main assumptions used in the modeling of ultrasound backscattering by RBCs are:

- The medium is weakly scattering (Born approximation). A weak scattering medium implies that multiple scattering does not significantly contribute to the backscattered power.
- There is no attenuation by the medium. Attenuation could be included in the model ($RF_{3D}(x, y, z) = e^{-\alpha(y)} \frac{\partial^2}{\partial y^2} T_{3D}(x, y, z) \otimes Z_{3D}(x, y, z)$, where α is the attenuation coefficient). However, this was not done because the attenuation as a function of the level of aggregation and scatterer's shape is not well characterized in the literature (especially at the ultrasound frequency and hematocrit considered in this study).
- The ultrasound beam is large enough that scatterers are small compared to the beam thickness, i.e., $T_z(-z)$ in (6) remains constant within each scatterer volume. For the simulation of RBC rouleaux, the change in the

scatterer volume was reflected in its length, and its diameter remained constant. For the RBC clump mimic, the diameter of the spherical clump increased with the scatterer volume. As described later, the largest clump diameters and longest rouleaux simulated had a dimension of 120 μm , which is still considerably smaller than the beam thickness of a typical ultrasound transducer that is about a millimeter. Thus, $T_z(-z)$ can be considered constant within each scatterer and it can be taken out of the integral in (6).

- All scatterers have an equal echogenicity a_n within the VOI.
- All scatterers have the same size, shape, and orientation. This simplifies the computation because it allows us to use a single scatterer prototype C for all particles. If a more realistic tissue image is required (i.e., a unique shape, size, and orientation for each scatterer), the method described in [15] can be used.

C. Implementation for Computer Simulations

The following steps can be used to implement the linear model of (2) on a computer:

Step 1. Create the PSF matrix $\frac{\partial^2}{\partial y^2} T(x, y)$, and rotate the PSF about the center of the matrix to simulate different angles of insonification (0 to 90°). The 3-D PSF was modeled by a Gaussian modulated cosine function:

$$T_{3D}(x, y, z) = e^{\left(-\frac{x^2}{2\psi_x^2} - \frac{y^2}{2\psi_y^2} - \frac{z^2}{2\psi_z^2}\right)} \cos(4\pi f y/c), \quad (11)$$

where ψ_x , ψ_y and ψ_z are the standard deviations of the Gaussian envelope controlling the beamwidth, the bandwidth (transmitted pulse length), and the beam thickness, respectively. A transducer beamwidth ($2\psi_x$) of 0.5 mm, a PSF length ($2\psi_y$) of 65.2 μm , and a transducer beam thickness ($2\psi_z$) of 0.5 mm were modeled¹. The parameters $2f/c$ in (11) represent the transducer spatial frequency, where f is the ultrasound frequency, and c is the speed of sound in blood. It is easy to show that the hypothesis of separability used to obtain (2) is valid for this PSF definition. In the present study, a transducer frequency (f) of 10 MHz and a speed of sound (c) of 1570 m/s were considered.

Based on the definition of (11), the PSF matrix $\frac{\partial^2}{\partial y^2} T(x, y)$ can be shown to be equal to:

$$\begin{aligned} \frac{\partial^2}{\partial y^2} T(x, y) &= T(x, y) \\ &\left[\left(\frac{y}{\psi_y^2}\right)^2 + \frac{(8\pi f y/c) \tan(4\pi f y/c) - 1}{\psi_y^2} - \left(\frac{4\pi f}{c}\right)^2 \right]. \end{aligned} \quad (12)$$

¹In this manuscript, the standard deviations used in the definition of the 3-D PSF (11) and scatterer prototype function (13) are used to approximate the radius of the dimension considered. For a Gaussian, 68.3% of the energy of the function is within the mean \pm one standard deviation. Thus, the true dimension is larger than the one defined here.

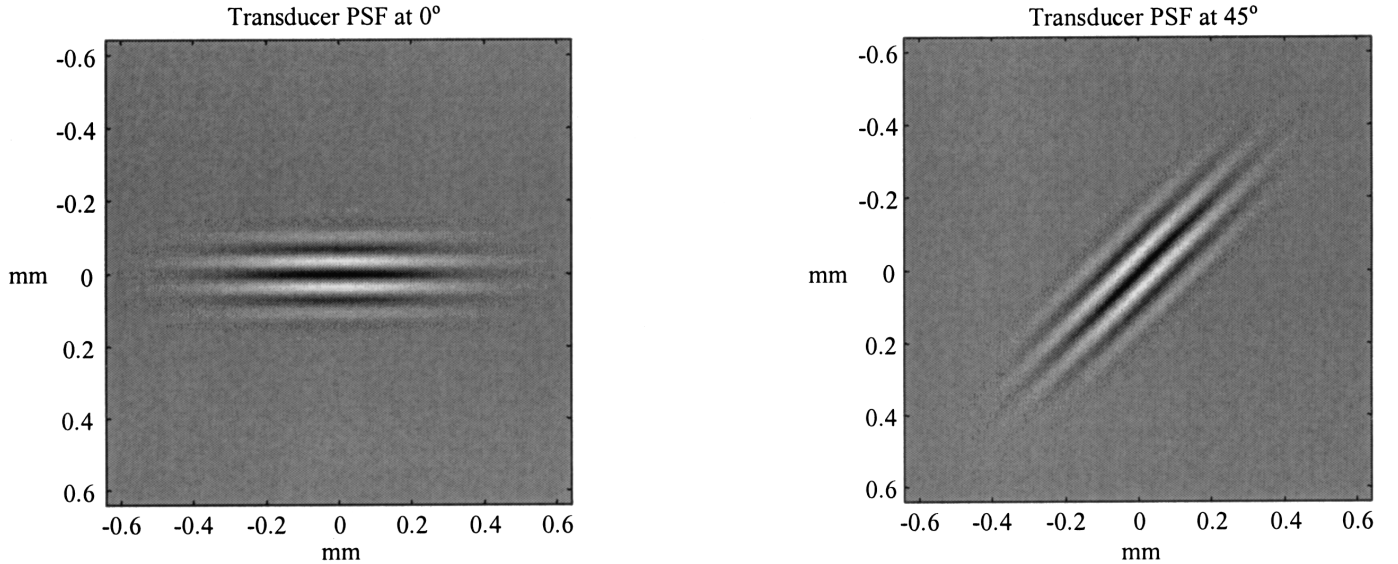


Fig. 1. The PSF used in the present study (12), for insonification angles of 0 and 45°.

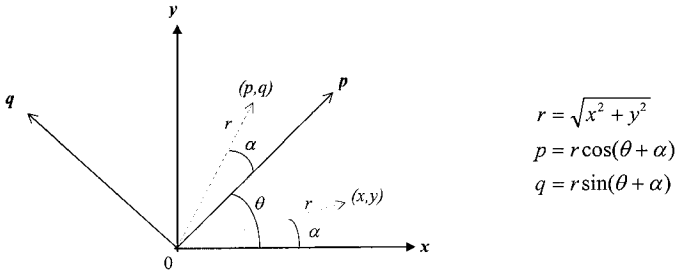


Fig. 2. Rotation of the $x - y$ plane about the z axis to simulate different insonification angles. The y axis represents the direction of propagation of the ultrasonic waves.

Fig. 1 shows the PSF defined by (12). Having obtained the PSF matrix, its rotation about the origin was accomplished by first rotating the axis by a desired angle, then implementing the function on the rotated axes, as shown in Fig. 2. Any arbitrary point on the $x - y$ plane was mapped onto the $p - q$ plane through the relationships shown in Fig. 2. Because the 2-D Gaussian function was applied onto the rotated axes, no interpolation was performed on the PSF matrix; therefore, no interpolation errors were introduced.

Step 2. Referring to (2), the objective is to create the tissue impedance function $Z(x, y)$, which is the convolution between the scatterer prototype function $C(x, y)$ and the position matrix $N(x, y)$ (9).

A 3-D separable Gaussian function was used to model $C_{3D}(x, y, z)$. This function was previously utilized to model biological tissues [16], [17]. The selection of this prototype tissue function allows modeling of isotropic and anisotropic scatterers of different sizes by simply modifying the dimension of the Gaussian function in the x , y , and z directions. This function also simplifies computation because the Fourier transform of a Gaussian is still a Gaussian in the frequency domain. According to (8), the

2-D Gaussian scatterer prototype was computed as:

$$C(x, y) = \sigma_z \sqrt{2\pi} e^{\left(-\frac{x^2}{2\sigma_x^2} - \frac{y^2}{2\sigma_y^2}\right)}, \quad (13)$$

where σ_x , σ_y , and σ_z are the standard deviations representing its width, length, and depth. Referring to (10), the scatterer position matrix $N(x, y)$ is a 2-D matrix with randomly positioned Dirac delta functions scaled by a_n and $T_z(-z_n)$, that are considered constant here. $T_z(-z_n)$ is supposed constant, not only within the scatterer volume, but also within the whole VOI. This is valid if one considers that scatterers are uniformly distributed along the z axis. If small pixel sizes are defined in the x and y directions, all scatterers are thus in phase with respect to the oscillations of the PSF, and their contribution can simply be added without using a specific weighting factor, $T_z(-z_n)$, for each scatterer. The function $N(x, y)$ was modeled as a Poisson distributed matrix modeling the random number of scatterers per pixel in the sample volume. The Poisson parameter (λ_p) was specified to consider a constant hematocrit of 10% ($\lambda_p = 0.10$ multiplied by the pixel volume, and divided by the volume of one scatterer). The pixel size and number considered are defined below.

Having created the scatterer position matrix $N(x, y)$, the tissue impedance function $Z(x, y)$ in (9) can be obtained by computing the product of the fast Fourier transform (FFT) of both $C(x, y)$ and $N(x, y)$ matrices, then computing the inverse FFT (IFFT) of the product. In order to minimize computation, the IFFT was not computed, and the tissue impedance, $Z(X, Y)$, was left in the frequency domain, where X and Y are the 2-D frequency variables.

Step 3. Following computation of (2) in the frequency domain to obtain $RF_{2D}(X, Y)$, the last step was to evaluate the backscattered power. The average power of the RF

image, in decibel (dB), was computed as follow:

$$POW_{av} = 10 \times \log_{10} \left[\frac{1}{M^2} \sum_{X_k=-M/2}^{M/2} \sum_{Y_k=-M/2}^{M/2} |RF_{2D}(X, Y)|^2 \right], \quad (14)$$

where M is the number of samples along each side of the image, and k is the frequency sample. The power on a linear scale also was computed for some figures. No normalization of the backscattered power was done. The IFFT of $RF_{2D}(X, Y)$ also was computed to obtain the B-mode image that is essentially the envelope of $RF_{2D}(x, y)$ (obtained by Hilbert transformation).

D. Simulated Conditions

Blood scatterers are usually moving in vivo. Such motion was not simulated, but it was indirectly considered because the movement of the fluid affects the shape, size, and orientation of the scatterers. Thus, simulating a snapshot of the scatterer positions may be consistent with reality. Simulating several snapshots for averaging purposes may reflect position changes of scatterers as a function of time, although no specific time-variation pattern was simulated in the present study. The size of the region of interest simulated was $1.28 \text{ mm} \times 1.28 \text{ mm}$, the number of pixels simulated was 512×512 , and the image resolution was $2.5 \mu\text{m}$ (which corresponds to a sampling frequency, $c/2$ divided by $2.5 \mu\text{m}$, of 314 MHz). The pixel size into which scatterers were positioned according to the Poisson distribution function had a volume of $3125 \mu\text{m}^3$ [$2.5 \mu\text{m} \times 2.5 \mu\text{m} \times 0.5 \text{ mm}(2\psi_z)$]. Note that the center of each scatterer is positioned not its entire volume. For all simulations, the hematocrit stayed constant at 10%.

Simulations were performed to evaluate the effect of the volume of scatterers and anisotropy due to their structure on the backscattered power. The signal power from two different sets of tissue matrices representing two different types of scatterer structures was compared: one was a group of isotropic scatterers (clumps); the other was anisotropic (rouleaux). Thirty tissue matrices for each set were generated to establish the error margin. All samples had the same scatterer size and hematocrit level; the only difference was the location of the scatterers, which was randomly distributed. For rouleaux, they were all aligned with the y axis (see Fig. 2). The power variation was examined at different insonification angles ranging from 0 to 90° . Note that at 0° , the direction of propagation is parallel to the long axis of rouleaux.

The scatterers in each set of tissue matrices were generated according to (13). Spherical clumps were modeled with identical standard deviations in the x , y , and z directions. Rouleaux were mimicked with the standard deviation in one direction greater than the others. More specifically, the width and depth of each rouleau, which is determined by σ_x and σ_z , were set to $7 \mu\text{m}$ (i.e., σ_x and σ_z were

both set to $3.5 \mu\text{m}$), whereas the length of each rouleau ranged from $4 \mu\text{m}$ to $120 \mu\text{m}$ (i.e. σ_y varied between $2 \mu\text{m}$ and $60 \mu\text{m}$). Because the thickness of a typical RBC is $2 \mu\text{m}$, this was to simulate a group of rouleaux, each consisting of 2 to 60 RBCs stacked together in the form of a rod. For RBC clump mimic, because a sphere is used to mimic this type of aggregates, σ_x , σ_y , and σ_z were all set equal. Values ranging from $2 \mu\text{m}$ to $60 \mu\text{m}$ (diameter = 4 to $120 \mu\text{m}$) were used. Fig. 3 shows one example of gray scale tissue images for each type of scatterer (rouleau lengths and clump diameters = $60 \mu\text{m}$), as well as the corresponding RF and B-mode images at 0° .

The simulated range of $4 \mu\text{m}$ to $120 \mu\text{m}$, the scatterer shapes selected and orientation for the case of rouleaux were solely for the purpose of examining the power for these conditions. These characteristics do not imply their physical existence physiologically. Such a range also was selected to observe the power in both Rayleigh and non-Rayleigh scattering situations. Rayleigh scattering occurs at particle sizes approximately less than one-tenth of the wavelength [13]. With the carrier frequency at 10 MHz and a sound velocity in blood at 1570 m/s, the corresponding wavelength is $157 \mu\text{m}$. Rayleigh scattering thus occurred only for clump diameters or rouleau lengths smaller than $15.7 \mu\text{m}$. The backscattered power estimated with our linear-system model recently showed good agreement with the T-matrix theory for nonaggregating spheres at high frequencies (non-Rayleigh scattering) [14]. Thus, the model should still be valid up to the dimension mentioned here, which is close to the size of the wavelength but no longer in the realm of Rayleigh scattering.

III. RESULTS

At a fixed hematocrit and similar spatial arrangement of scatterers, a linear relationship is expected under Rayleigh scattering (scatterer' sizes $< 15.7 \mu\text{m}$) between the signal power and the particle volume for the linear model to be valid. For the first series of simulation, the diameter of the clump mimics was preset to range from 4 to $13 \mu\text{m}$, at $1 \mu\text{m}$ increment. This corresponded to σ_x , σ_y , and σ_z varying from 2 to $6.5 \mu\text{m}$, and an approximate range of scatterer volume from 34 to $1150 \mu\text{m}^3$, respectively. The length of the rouleau mimics was also preset to the same range (σ_y varying from 2 to $6.5 \mu\text{m}$) with the corresponding scatterer volume ranging from 154 to $500 \mu\text{m}^3$. Fig. 4 presents the power versus volume relationship for the RBC clump and rouleau mimics. As shown, linear relationships were obtained for the scatterer volumes considered. For a given scatterer volume, the power was higher for the clump mimics compared to the rouleau mimics.

Fig. 5 shows the mean backscattered power as a function of the angle of insonification, for rouleau lengths and clump diameters of $60 \mu\text{m}$ (non-Rayleigh scatterers). From this graph, it is apparent that the difference in the scatterer shape is reflected in the power with this model. A change of approximately 25 dB in the mean power for RBC rouleau mimics was observed as a function of the angle. As

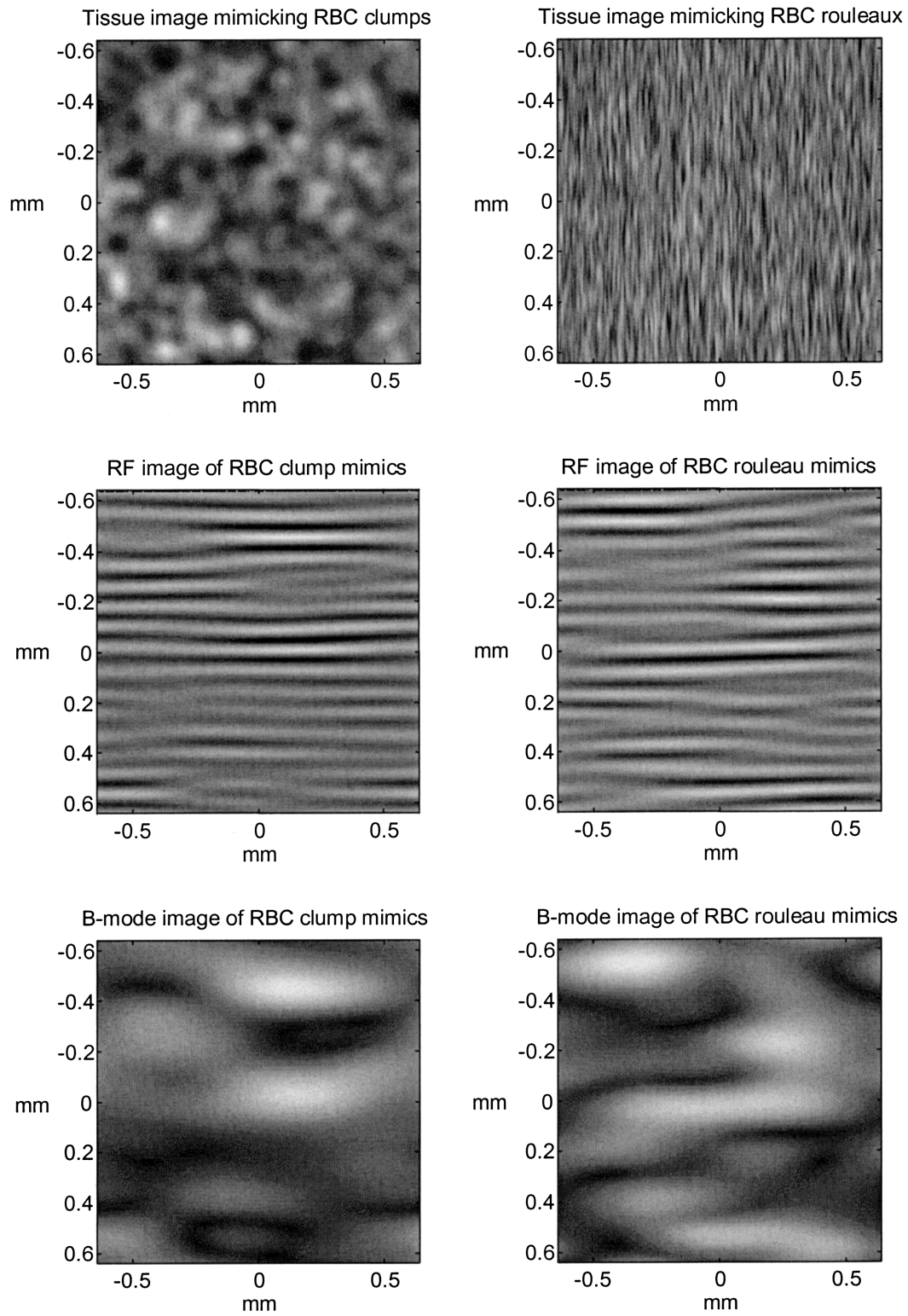


Fig. 3. Examples of tissue images $Z(x, y)$, RF images $RF_{2D}(x, y)$, and B-mode images of RBC clump and rouleau mimics, at an angle of 0° and a hematocrit of 10%. For RBC rouleaux, scatterers are aligned parallel to the y axis.

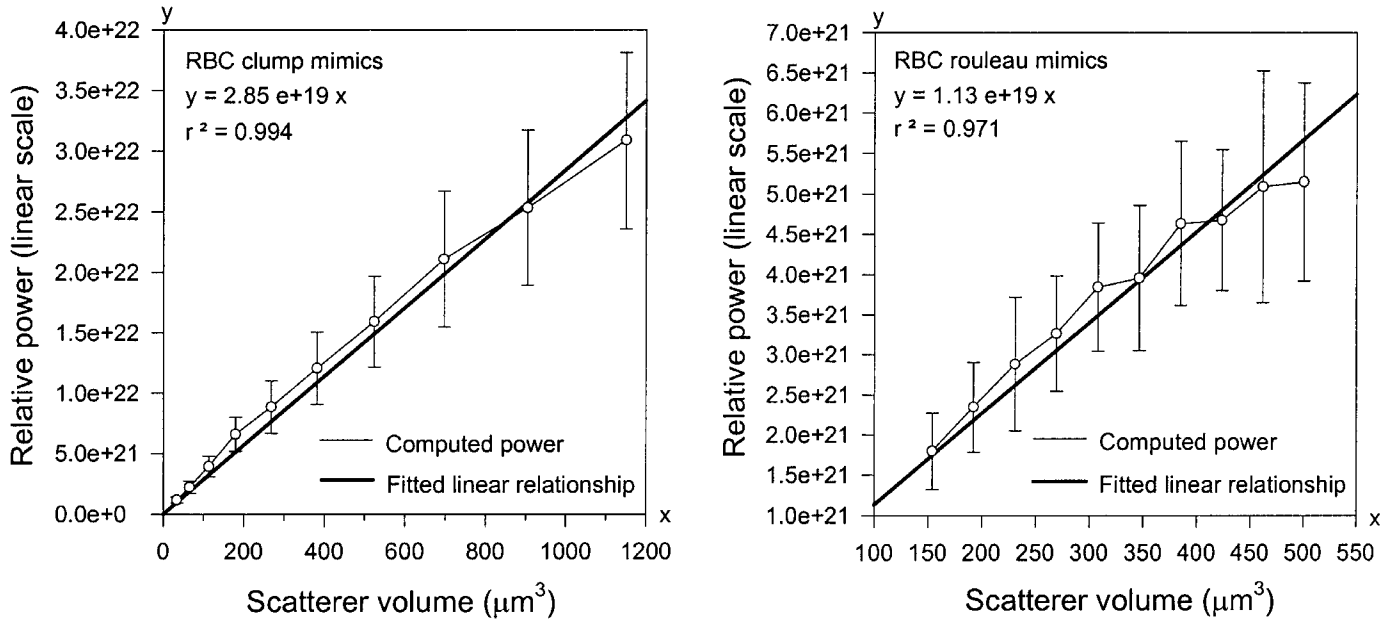


Fig. 4. Linear power-volume relationships for isotropic spherical clumps and anisotropic cylindrical rouleaux, at an angle of 0° . The error bars for each scatterer size represent one standard deviation obtained from 30 tissue matrices. The correlation coefficients (r^2) were fitted onto the mean backscattered power values.

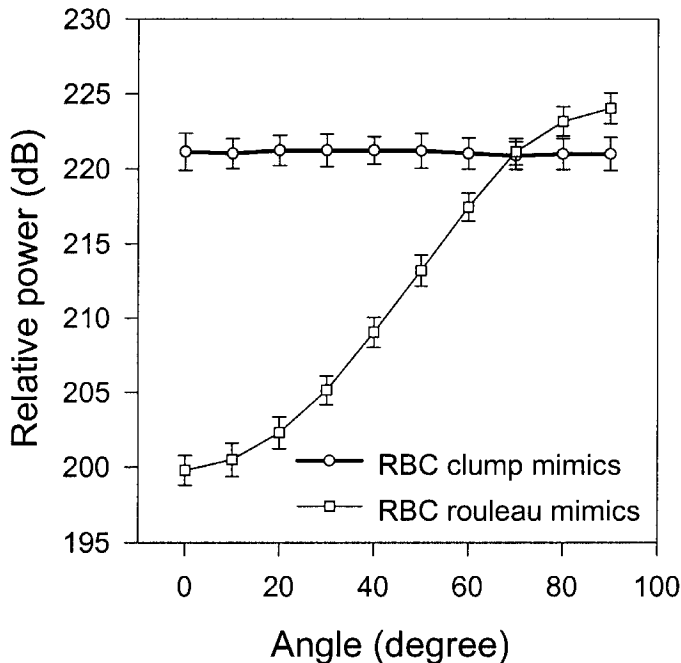


Fig. 5. Comparison of the mean backscattered power between simulations of RBC clumps (60 μm in diameter) and rouleaux (60 μm in length). The error bars for each angle represent one standard deviation obtained from 30 tissue matrices.

expected, no change in the mean power was found for the RBC clumps.

To further elucidate the role of the scatterer size and shape on the backscattered power, 30 different scatterer volumes were simulated over dimensions (σ) varying between 2 and 60 μm . Both σ_x and σ_z remained at 3.5 μm for the rouleau mimics, and the change in volume was re-

flected in σ_y . As performed before, σ_x , σ_y , and σ_z all had identical values for the clump mimics. Fig. 6 shows results for the range of sizes considered, and insonification angles of 0° , 22.5° , 45° , 67.5° , and 90° . One can see that the signal power increases up to a peak as the scatterer size increases, but any further increase in the diameter or length of the scatterers results in a decrease in the signal power, except when the scatterer structure is in the form of a rouleau at the insonification angle of 90° . In this case, the signal power continues to increase with the scatterer length (it is expected to drop for longer rouleaux when the size exceeds the ultrasound beam thickness). For RBC rouleau mimics, the position of the peak is also changed, depending on the insonification angle; and the differences across the insonification angles appear to be enhanced for longer rouleaux. For spherical clumps, no anisotropy was observed as expected.

IV. DISCUSSION

A. Influence of the Scatterer Size on the Backscattered Power

Generally, the backscattered power in Fig. 6 increased up to a peak then decreased as the scatterer volume continued to increase. Such behavior can be better understood in the frequency domain. The convolution operation described in (2) is the multiplication, in the frequency domain, of the Fourier transform of the PSF with the Fourier transform of the tissue image. Fig. 7 shows the magnitude spectrum of the PSF at an arbitrary insonification angle of 0° . The position of the two spots on the 2-D spectrum is at the carrier frequency of the PSF (10 MHz). The

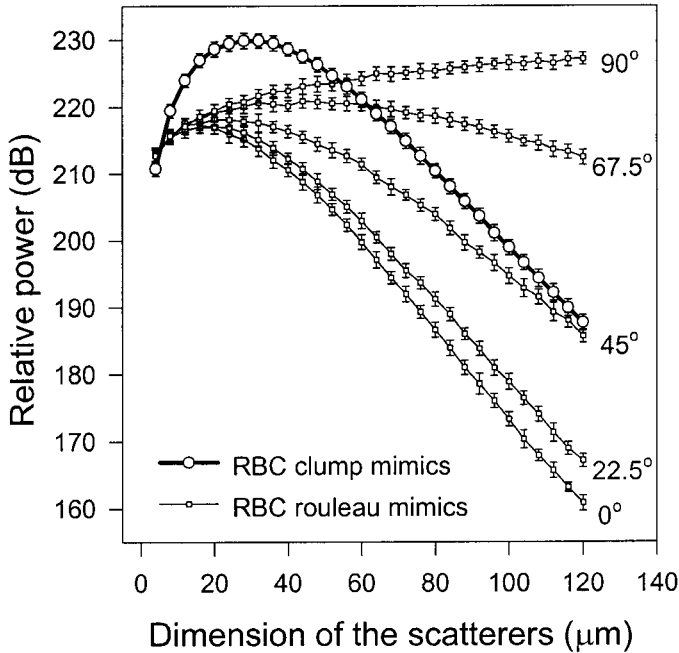


Fig. 6. Power versus dimension (diameter for clumps and length for rouleaux) of RBC mimicking aggregates. The data are for 5 different insonification angles (0, 22.5°, 45°, 67.5°, and 90°). Because no angular dependence was found for RBC clump mimics, all data were pooled and plotted as one curve. The error bars for each scatterer size represent one standard deviation obtained from 30 tissue matrices.

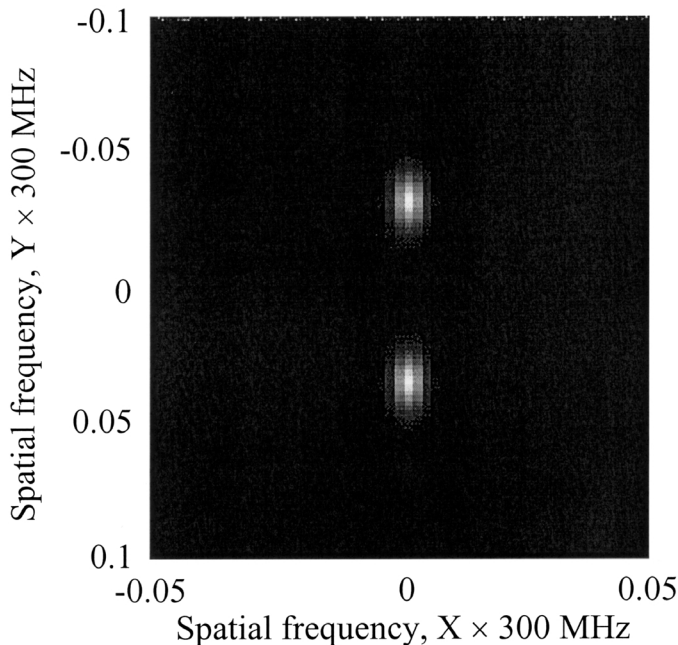


Fig. 7. Magnitude spectrum of the transducer PSF in Fig. 1 for an insonification angle of 0°.

right panels of Figs. 8 and 9 present the magnitude spectrum of the tissue images shown on the left panels, for RBC clumps with diameters of 20 μm and RBC rouleau mimics with a length of 20 μm . These spectra are essentially matrices with 2-D delta functions weighted by the scatterer prototype function (9). According to (2), the backscattered power is determined by the overlapping area between the PSF spectrum (Fig. 7) and the tissue image spectrum (right panels of Figs. 8 and 9).

From the Fourier transform relationship between space and frequency, scaling in the spatial domain leads to an inverse relationship in the frequency domain [18]:

$$f(ax) \xleftrightarrow{FT} \frac{1}{|a|} F\left(\frac{\omega}{a}\right) \quad (15)$$

where $f(ax)$ is the function in the spatial domain, a is the scaling factor, x is the spatial domain variable, FT is the Fourier transform, F is the function in the frequency domain, and ω is the frequency domain variable. As the scatterer size is increased along a given direction in the spatial domain ($a < 1$) in (15), the tissue image spectrum shrinks along the same direction in the frequency domain, and its amplitude increases. However, if the scatterer size is reduced in one direction ($a > 1$), the spectrum of the tissue image expands in the same direction, and the amplitude decreases. For small scatterers, as the size is increased the increase in the amplitude of the spectrum offsets such scaling effect in the frequency domain; as a result, the backscattered power is increased as observed in Fig. 4 for Rayleigh scattering. As the scatterer size continues to increase, the overlapping region between the PSF spectrum and the tissue image spectrum is reduced, leading to a decrease in backscattered power. For the particular case of rouleau mimics, the tissue spectrum has the form of an ellipsoid. Because the diameter of rouleaux is kept constant for all simulations, the bandwidth of the spectrum along the X frequency axis is unchanged when the scatterer size is increased. Shrinking of the spectrum only occurs along the Y frequency axis. When the rouleau size is reduced, the ellipsoid in the spectrum of the tissue image tends to be circular.

In general, as the scatterer size is increased, one can conclude that the backscattered power depends on the increase in amplitude of the tissue spectrum, the decrease in the overlapping region with the PSF spectrum, and the number of scatterers in the region of interest. The number of scatterers in the region of interest for large scatterers is not as numerous as when the scatterers are smaller, because the hematocrit is kept constant. As a consequence, this effect may also contribute to the reduction of the backscattered power at high scatterer sizes.

B. Effect of the Insonification Angle on the Backscattered Power

In the model, the change in the insonification angle was represented by the rotation of the PSF about its origin, which is the center of the image. In the frequency domain,

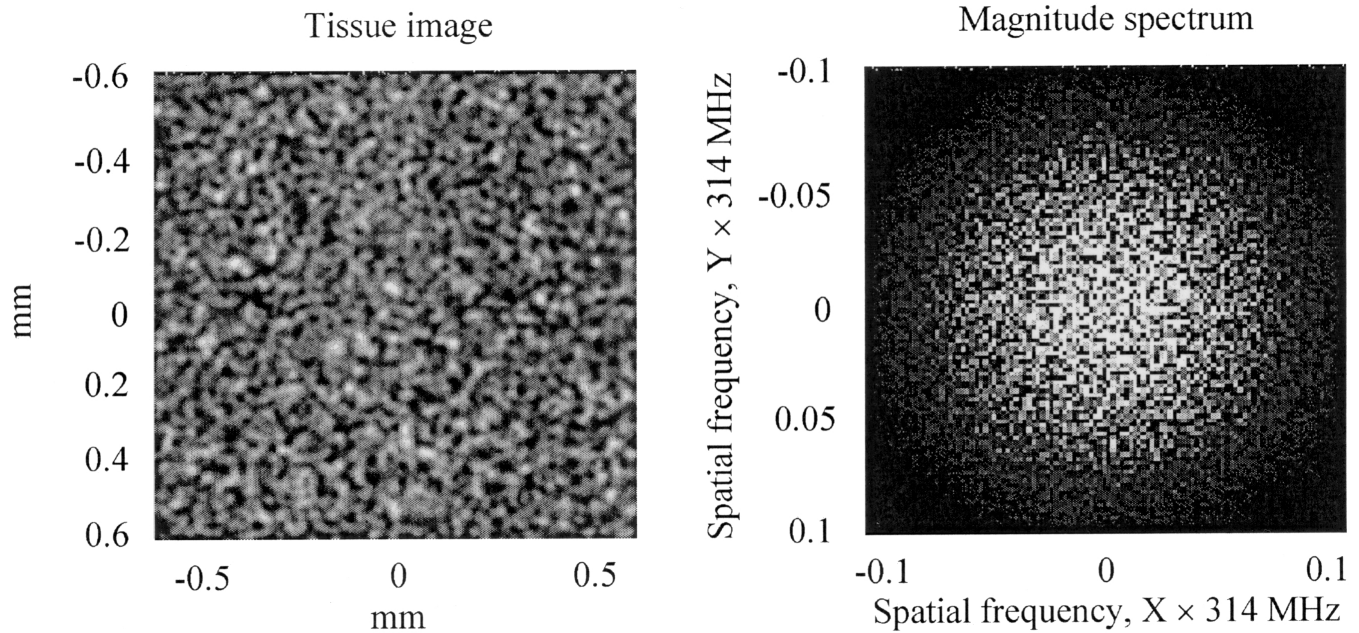


Fig. 8. Tissue matrix mimicking RBC clumps of $20\ \mu\text{m}$ diameter at 10% hematocrit with the corresponding magnitude spectrum. Note that the DC component has been removed from the spectrum for better visualization.

rotating the PSF produces a rotation of the two spots shown in Fig. 7. From the spectrum in Fig. 8, it is not difficult to see that the backscattered power from such a tissue mimic is angular independent because the isotropic structure of the scatterers is reflected in the frequency domain. As the PSF is rotated across the different insonification angles, the symmetry of the tissue image spectrum causes the overlapped region with the PSF spectrum to remain unchanged, leading to the angular-independent backscattered power.

According to Fig. 6 for rouleau mimics, increasing the angle leads to an increase of the backscattered power. This can be explained by the fact that the two spots on the PSF spectrum increasingly overlap with the region occupied by the ellipsoidal tissue image spectrum as the angle is changed from 0 to 90° . Note that at 90° , the power drop is not observed because the volume change of the rouleau mimics is reflected in the length, which is along the y axis. In the frequency domain, the change in the scatterer volume does not affect the overlapping region between both spectra because the two spots of the PSF are aligned along the x axis and superimposed over the tissue spectrum. Thus, the increase in amplitude of the tissue spectrum as the rouleau length is increased raises the backscattered power.

C. Comparison of the Simulated Results

To our knowledge, modeling of blood backscattering by RBC aggregates has not been attempted before. Kumar and Mottley [19] proposed a time-domain Born approximation model to predict the anisotropy of ultrasound backscattering from myocardial muscular fibers. They modeled the differential backscattering cross section from one fiber of different lengths, as a function of the in-

sonification angle. The anisotropy was not significant between 2 and $8\ \text{MHz}$ for a length of $41\ \mu\text{m}$. However, for fibers of 80 and $102\ \mu\text{m}$, the backscattered power was maximum at 90° and minimum at 0° for frequencies above $4\ \text{MHz}$. In the non-Rayleigh region (higher frequencies), the power continued to increase with frequency at 90° and 60° , and dropped at 30° and 0° . In Fig. 6, a similar behavior was found at $10\ \text{MHz}$ in the non-Rayleigh region (longest rouleau mimics). For instance, the backscattered power increased as the rouleau length was raised for an angle of 90° , whereas it decreased for all other angles. In [19], the backscattering coefficient at $8\ \text{MHz}$ was plotted as a function of the angle of insonification θ . The backscattering coefficient varied as $\sin(2\theta - 90^\circ)$, which is similar to the variation observed in Fig. 5 for the rouleau mimics. It is interesting to note that similar results were also obtained analytically by Insana [17]. In that study, a transverse isotropic correlation model was developed to explain the anisotropy of the kidney microstructure. The integrated backscatterer coefficient varied sinusoidally with the angle of insonification, at frequencies ranging between 2.5 and $5\ \text{MHz}$, and 5 and $15\ \text{MHz}$.

D. Other Considerations

It is important to note that the position of the peaks observed in Fig. 6 is dependent on the carrier frequency of the PSF. In this study, a PSF carrier frequency of $10\ \text{MHz}$ was used for all simulations. However, the peak would be expected to occur at a larger scatterer size if the carrier frequency had been reduced, and vice versa. From a physical point of view, lower carrier frequency implies greater wavelength, which means that larger scatterers can be considered as Rayleigh scatterers.

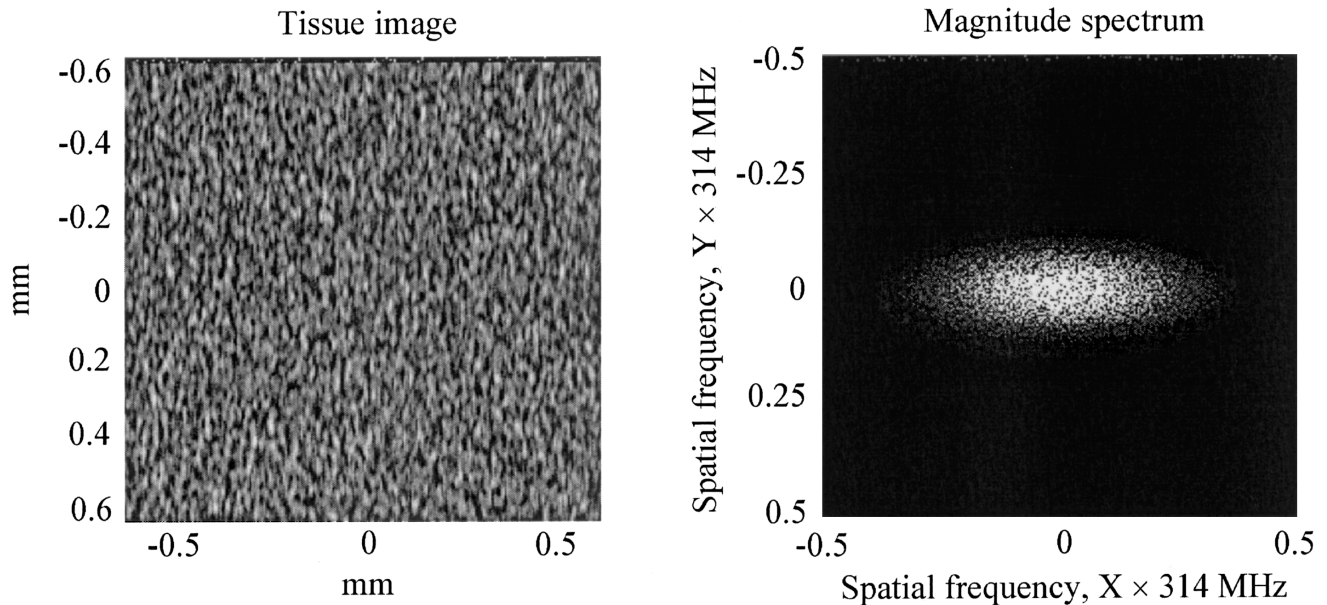


Fig. 9. Tissue matrix mimicking RBC rouleaux of $20 \mu\text{m}$ length at 10% hematocrit with the corresponding magnitude spectrum. Note that the DC component has been removed from the spectrum for better visualization. The RBC rouleaux are aligned parallel to the y axis.

With regard to the effects of the system parameters toward the backscattered power, the bandwidth and beamwidth of the ultrasound system, which corresponds respectively to the standard deviations ψ_y and ψ_x in (11), are also important because both variables affect the spectrum of the PSF. However, any power variations due to these system parameters will not affect the trend of the backscattered power observed in Figs. 4 to 6.

In this study, the pixel size into which scatterers were positioned according to the Poisson distribution function had a volume of $3125 \mu\text{m}^3$ ($2.5 \mu\text{m} \times 2.5 \mu\text{m} \times 0.5 \text{mm}$). The distribution used is dependent on the number of scatterers per pixel. For a fixed hematocrit level of 10%, the scatterer number per pixel is generally less than 12 (for scatterers greater than $4 \mu\text{m}$ in length or diameter), which can be adequately modeled by the Poisson distribution. However, this probability distribution function would not be appropriate to study higher hematocrits because scatterers become correlated. In this case, a Gaussian statistical distribution function may be more appropriate to distribute the number of scatterers per pixel, as used in another study [14]. The parameters of the Gaussian model as a function of the level of RBC aggregation remain to be studied.

The linear relationships obtained in Fig. 4 between the signal power and the scatterer's volume may not be reproducible at a hematocrit higher than 10%. One hypothesis that has to be respected for this situation to exist is the presence of a similar spatial arrangement of scatterers between each step change in volume. By considering a low hematocrit, the packing arrangement of scatterers was kept unchanged for the range of volume considered, and linear relationships were obtained in Fig. 4. However, in the presence of physiological RBC aggregation under flowing condition, different aggregate packing organization

may exist even if the hematocrit is low and kept constant. This would have to be considered to simulate a more realistic physiological situation. Moreover, because rouleaux are not expected to be perfectly aligned in the human circulatory system, a larger variance is anticipated for measurements such as those in Figs. 5 and 6.

As shown in (13), 3-D Gaussian-shaped scatterers were used in this study. Because the transducer may not be able to resolve the edges of scatterers, and because the acoustic impedance of RBCs (density and compressibility) may not be uniform within the cell and higher near the center, a function that decays smoothly may be a good approximation. In a recent study [14], we used both Gaussian and spherical scatterer prototypes to describe the shape of the RBC. For the Gaussian isotropic prototype, the backscattered power decayed as in Fig. 6 for non-Rayleigh scattering. However, the power oscillated around a mean value for spherical scatterers. Based on the current knowledge, it is difficult to determine the appropriate scatterer prototype. For instance, no experimental data is available, to our knowledge, to compare our results for non-Rayleigh scattering.

In this study, two or more scatterers may overlap on top of one another when the 3-D matrix is projected along the z axis and is collapsed into a 2-D version in (2). Note that, even though scatterers may overlap, the contribution of each of them on the backscattered power is considered in the model. Moreover, because scatterers are sampled in 2-D with a resolution of $2.5 \mu\text{m}$, acoustic interference within each scatterer is also considered with the model. In the 2-D convolution of (2), the phase of the PSF in the volume of interest determines the effect, on the backscattered power, of constructive or destructive echoes produced from the different point sources.

V. CONCLUSION

In a recent study [14], a comparison of the simulation results to theoretical predictions and experimental results reported in the literature validated the linear-system model. In that study, computer simulations of the model were used to study the power backscattered by non-aggregating RBCs as a function of the hematocrit, the volume of the scatterers, and the frequency of the incident wave. The current study is a first attempt aiming to evaluate the effect of RBC aggregation on the backscattered power. The modeling of the tissue function with identical clumps and rouleaux, all oriented with the y axis for the rouleaux, does not reflect physiological condition. Under in vivo flowing condition, polydispersity in size, shape, and orientation is expected. Due to the complexity of ultrasound backscattering by blood, the strength of the current approach is the possibility of studying individually the effect, on the backscattered power, of variables such as the scatterer size, shape, and insonification angle. In contradiction to what would be expected from the Rayleigh scattering theory [13], the model predicts that the ultrasound backscattered power may not always increase with the size of the aggregates, especially when they are no longer Rayleigh scatterers. It was also observed from this study that the anisotropy of the backscattered power is emphasized in the non-Rayleigh region.

ACKNOWLEDGMENT

The authors gratefully acknowledge Dr. Michel Bertrand of the Institute of Biomedical Engineering, École Polytechnique of Montreal for training Mr. Teh with the linear-system model, and Mrs. Isabelle Fontaine and Mr. David Savéry for reviewing the manuscript.

REFERENCES

- [1] S. Chien, "Biophysical behavior of red cells in suspensions," in *The Red Blood Cell*, D. M. Surgenor, Ed. New York: Academic, 1975, pp. 1031–1133.
- [2] H. I. Bicher, *Blood Cell Aggregation in Thrombotic Processes*. Springfield: IL, 1972, pp. 1–177.
- [3] G. Cloutier and Z. Qin, "Ultrasound backscattering from non-aggregating and aggregating erythrocytes—A review," *Biorheology*, vol. 34, pp. 443–470, 1997.
- [4] Y. W. Yuan and K. K. Shung, "Ultrasonic backscatter from flowing whole blood. I: Dependence on shear rate and hematocrit," *J. Acoust. Soc. Amer.*, vol. 84, pp. 52–58, 1988.
- [5] —, "Ultrasonic backscatter from flowing whole blood. II: Dependence on frequency and fibrinogen concentration," *J. Acoust. Soc. Amer.*, vol. 84, pp. 1195–1200, 1988.
- [6] S. Y. Kim, I. F. Miller, B. Sigel, P. M. Consigny, and J. Justin, "Ultrasonic evaluation of erythrocyte aggregation dynamics," *Biorheology*, vol. 26, pp. 723–736, 1989.
- [7] M. Boynard and J. C. Lelièvre, "Size determination of red blood cell aggregates induced by dextran using ultrasound backscattering phenomenon," *Biorheology*, vol. 27, pp. 39–46, 1990.
- [8] J. G. Mottley and J. G. Miller, "Anisotropy of the ultrasonic backscatter of myocardial tissue: I. Theory and measurements in vitro," *J. Acoust. Soc. Amer.*, vol. 83, pp. 755–761, 1988.
- [9] T. M. Burke, E. L. Madsen, and J. A. Zagzebski, "A preliminary study on the angular distribution of scattered ultrasound from bovine liver and myocardium," *Ultrason. Imag.*, vol. 9, pp. 132–145, 1987.
- [10] B. K. Hoffmeister, A. K. Wong, E. D. Verdonk, S. A. Wickline, and J. G. Miller, "Comparison of the anisotropy of apparent integrated ultrasonic backscatter from fixed human tendon and

- fixed human myocardium," *J. Acoust. Soc. Amer.*, vol. 97, pp. 1307–1313, 1995.
- [11] M. F. Insana, T. J. Hall, and J. L. Fishback, "Identifying acoustic scattering sources in normal renal parenchyma from the anisotropy in acoustic properties," *Ultrason. Med. Biol.*, vol. 17, pp. 613–626, 1991.
- [12] L. Allard, G. Cloutier, and L. G. Durand, "Effect of the insonification angle on the Doppler backscattered power under red blood cell aggregation conditions," *IEEE Trans. Ultrason., Ferroelect., Freq. Contr.*, vol. 43, pp. 211–219, 1996.
- [13] K. K. Shung and G. A. Thieme, *Ultrasonic Scattering in Biological Tissues*, Boca Raton, FL: CRC Press, 1993, pp. 1–486.
- [14] I. Fontaine, M. Bertrand, and G. Cloutier, "A system-based approach to modeling the ultrasound signal backscattered by red blood cells," *Biophysical J.*, vol. 77, pp. 2387–2399, 1999.
- [15] B. G. Teh, "The modeling and analysis of ultrasound backscattering by red blood cell aggregates with a system-based approach," 1998, M.Eng. thesis, McGill Univ., Montreal, P.Q., Canada, pp. 1–89.
- [16] J. Meunier and M. Bertrand, "Echographic image mean gray level changes with tissue dynamics: A system-based model study," *IEEE Trans. Biomed. Eng.*, vol. 42, pp. 403–410, 1995.
- [17] M. F. Insana, "Modeling acoustic backscatter from kidney microstructure using an anisotropic correlation function," *J. Acoust. Soc. Amer.*, vol. 97, pp. 649–655, 1995.
- [18] A. V. Oppenheim, A. S. Willsky, and I. T. Young, *Signals and Systems*, Englewood Cliffs, NJ: Prentice-Hall, 1983, pp. 1–766.
- [19] K. N. Kumar and J. G. Mottley, "Quantitative modeling of the anisotropy of ultrasonic backscatter from canine myocardium," *IEEE Trans. Ultrason., Ferroelect., Freq. Contr.*, vol. 41, pp. 441–451, 1994.



Beng-Ghee Teh was born in Penang, Malaysia. He received the B.Eng. and M.Eng. degrees in electrical engineering in 1994 and 1998 respectively, from McGill University and the Clinical Research Institute of Montreal, Montreal, Quebec, Canada. He is currently an Applications Engineer at Cypress Semiconductor in San Jose, California, where he is involved with the definition, development, test and support of data communications products.



Guy Cloutier (S'89–M'90) obtained his B.Eng. degree in electrical engineering from the Université du Québec à Trois-Rivières in 1983, and his M.Sc. and Ph.D. degrees in biomedical engineering from the École Polytechnique of Montreal in 1986 and 1990, respectively. Between 1990 and 1992, he pursued postdoctoral training with Dr. K. Kirk Shung at the Laboratory of Medical Ultrasonics, Bioengineering Program, The Pennsylvania State University.

Dr. Cloutier currently is director of the Laboratory of Biorheology and Medical Ultrasonics at the Research Center of the University of Montreal Hospital, visiting scientist at the Laboratory of Biomedical Engineering of the Clinical Research Institute of Montreal, and associate professor in the Department of Radiology and Institute of Biomedical Engineering, Faculty of Medicine, University of Montreal.

His research interests are the characterization of red blood cells aggregation dynamics with ultrasound, the 3-D morphologic and hemodynamic assessment of lower limb arterial stenoses with Doppler ultrasound, and the quantification of the effect of blood flow turbulence on the dysfunction of prosthetic heart valves. He has published more than 50 papers and book chapters in these fields. Dr. Cloutier is the recipient of research scholarships from the Fonds de la Recherche en Santé du Québec since 1992.